

Nonperturbative calculation of exchange coupling parameters

Tomonori Tanaka* and Yoshihiro Gohda†

Department of Materials Science and Engineering, Institute of Science Tokyo, Yokohama 226-8501, Japan

(Dated: March 20, 2025)

Exchange coupling parameters J_{ij} within the Heisenberg model and its extensions are crucial for understanding magnetic behavior at the atomic level. To calculate J_{ij} from first principles, perturbative methods based on the magnetic force theorem (MFT), commonly referred to as Liechtenstein's method, have been widely employed. However, the quantitative accuracy of J_{ij} obtained through this perturbative technique remains uncertain. In this paper, we nonperturbatively calculate J_{ij} for several systems of both fundamental and applied significance, including perovskite SrMnO₃, neodymium-magnet compounds, and elemental 3*d* transition metals, and compare these results with those obtained using the conventional MFT-based method. The nonperturbative approach provides consistent results for magnetic configurations exhibiting a certain degree of magnetic disorder. In contrast, due to its inherent theoretical limitations, the MFT-based method struggles to accurately evaluate the magnetic energy in such configurations. As discussed later in this paper, these discrepancies arise from neglected contributions within MFT-based methods. Our nonperturbative scheme is highly versatile and holds strong prospects as a new platform for analyzing and designing spintronic materials, where developing accurate spin models is essential.

I. INTRODUCTION

Understanding magnetic interactions at the atomic level has become increasingly important with recent advancements in spintronics technology [1]. Currently, density functional theory (DFT) is the standard method for electronic structure calculations and effectively meets these quantitative demands. However, DFT is inherently valid only for ground-state properties. Therefore, to simulate magnetic states at finite temperatures and spin dynamics phenomena such as skyrmions and magnons, which are essential for practical applications, more coarse-grained computational models are required. One such approach is the lattice-spin model [2].

The lattice-spin model is a framework that focuses exclusively on spin degrees of freedom, excluding charge degrees of freedom, with the Heisenberg model and its extensions serving as representative examples. The quantitative accuracy of such models is determined by their parameters, including the exchange coupling parameters J_{ij} . Today, the evaluation of J_{ij} in the Heisenberg model from first principles has become common practice [3, 4]. The most widely used method for determining J_{ij} is Liechtenstein's method, which is based on perturbation theory [5, 6] referred to as the magnetic force theorem (MFT). The conventional MFT-based methods and their variants [3, 4, 7–10] have been applied to a wide range of magnetic materials, providing microscopic insights into interatomic magnetic interactions. However, recent theoretical studies have highlighted discrepancies between J_{ij} values obtained from MFT-based methods and those derived from nonperturbative (self-consistent) calculations in certain materials, even for relatively small rotation angles of magnetic moments [11, 12]. A particularly noteworthy case is SrMnO₃ in the type-G antiferromagnetic state, where the first-nearest-neighbor J_{ij} values obtained from an MFT-based method and self-consistent calculations were found to have opposite signs

[12]. This example raises concerns about the straightforward applicability of MFT.

The fundamental principle of MFT within DFT is based on the energy variation δE due to the infinitesimal rotations of magnetic moments as [13]

$$\begin{aligned}\delta E &= \delta^* E_{\text{band}} + \mathcal{O}(\delta n^2, \delta m^2) \\ &\approx \delta^* E_{\text{band}},\end{aligned}\quad (1)$$

where δn and δm represent changes in electron density and the longitudinal change in magnetization density, respectively. Here, $\delta^* E_{\text{band}}$ refers to the variation in band energy under conditions of fixed electron density and fixed magnetization magnitude, where only the direction of the magnetization is rotated. According to Eq. (1), MFT-based methods consider only the change in $\delta^* E_{\text{band}}$. The term $\mathcal{O}(\delta n^2, \delta m^2)$, which consists of second order variations of the band energy and double-counting terms, can be neglected for infinitesimal rotations. Although this approximation is formally exact for infinitesimal rotations, its validity must be reassessed for a more accurate description of finite-temperature magnetism, as the magnetic states of interest typically involve finite rotation angles.

In this study, we demonstrate the importance of a nonperturbative evaluation of J_{ij} by applying it to several systems. The selected systems include perovskite SrMnO₃ and neodymium-magnet compounds, where conventional MFT-based methods have shown some inaccuracies, and elemental 3*d* transition metals. As pointed out in Ref. [12], a conventional MFT-based method cannot reproduce the energy variation due to small rotations of magnetic moments in perovskite SrMnO₃ with the type-G antiferromagnetic state. In contrast, J_{ij} obtained through the nonperturbative method does not exhibit this inconsistency. We reveal that the discrepancy between the two methods stems from significant changes in orbital occupations, which are difficult to capture using MFT-based methods (Sec. IV A). We also calculate the Curie temperatures (T_C) of Nd₂Fe₁₄B and Nd₂Co₁₄B as representative permanent magnet compounds. It has been reported that an MFT-based method failed to reproduce the experimental results showing

* tanaka.t.da74@m.isct.ac.jp

† gohda@mct.isct.ac.jp

an increase in the T_C with Co substitution in these permanent magnet compounds [14]. We demonstrate how the nonperturbative method consistently produces results that align with the experimental findings without contradictions (Sec. IV B). In Sec. IV C, we systematically calculate J_{ij} for elemental 3d transition metals with bcc and fcc structures and compare these results with those obtained using an MFT-based method. We find that the contribution of $\mathcal{O}(\delta n^2, \delta m^2)$ is not negligible for quantitative evaluations of J_{ij} , even with relatively small rotation angles of magnetic moments. A key focus of this study is the contribution of $\mathcal{O}(\delta n^2, \delta m^2)$. Therefore, in Sec. V, we discuss the concept of $\mathcal{O}(\delta n^2, \delta m^2)$ in detail.

II. METHODS

A. Nonperturbative calculation of J_{ij} with supercells

The validity of an effective spin model depends on the symmetry of the system and the required energy accuracy. We use a classical spin model consisting of the lowest-order pairwise interactions throughout this study as

$$E(\{\hat{e}\}) = E_0 - \sum_{i \neq j} J_{ij} \hat{e}_i \cdot \hat{e}_j, \quad (2)$$

where E_0 is the reference energy, J_{ij} is the isotropic exchange coupling parameter between site i and j , and \hat{e}_i is a unit vector representing the orientation of the local magnetic moment on site i . This simplified model is valid when the influence of the anisotropy of the system on the physical quantities of interest is small. The model parameters J_{ij} and E_0 can be determined by minimizing the residual sum of squares [15] defined as

$$\Delta E^2 = \frac{1}{N_{\text{data}}} \sum_{n=1}^{N_{\text{tot}}} \left(E_{\text{DFT}}^{(n)} - E_{\text{model}}^{(n)} \right)^2, \quad (3)$$

where $E_{\text{DFT}}^{(n)}$ is the energy obtained from DFT calculations for n -th magnetic configuration, $E_{\text{model}}^{(n)}$ is the energy related to the spin model, and N_{data} is the total number of magnetic configurations. In this study, we used the supercell method to model magnetic configurations. Therefore, we hereinafter refer to this procedure as the (SC)² method (Self-Consistent SuperCell method) for convenience. In the practical calculations, we used the symmetry of the target systems to identify independent J_{ij} by using Spglib library [16].

The model parameters in Eq. (2) depend on how the magnetic configuration dataset is sampled. Our focus is on J_{ij} near stable or metastable magnetic configurations to compare them with those obtained from MFT-based methods. Therefore, we slightly tilted the direction of the magnetic moment on each atom from a (meta)stable magnetic configuration. Specifically, we used uniformly distributed random numbers on a spherical cap in the range of $0^\circ \leq \theta \leq \theta_{\text{max}}$ by using inversion transform sampling, while azimuthal angles were unrestricted. Magnetic configurations were sampled until the parameters converged; typically, three times the number of independent J_{ij} magnetic configurations were used. The above sampling procedure leads

to the dependence of J_{ij} on θ_{max} . This dependence arises from changes in the electronic structure resulting from thermally induced magnetic disordering. Consequently, the dependence of J_{ij} on θ_{max} provides insight into how J_{ij} and the resulting theoretical magnetic phase transition point vary with temperature. This will be revisited in the discussion of T_C in Nd₂Fe₁₄B and Nd₂Co₁₄B (Sec. IV B). If we wish to eliminate the parameter θ_{max} , a more refined sampling approach may be required. For example, in Ref. [17], magnetic configurations at finite temperatures are sampled using a combination of Monte Carlo simulations.

We note that the parameters J_{ij} in the (SC)² method involve a size effect similar to that in the direct method for phonon calculations; the parameters are not values between individual sites but between the periodic images of sites i and j . This size effect decreases as the supercell size increases. Therefore, we carefully check the convergence of J_{ij} with respect to the supercell size. Additionally, we distinguish the (SC)² method from approaches that rely on energy differences between completely different magnetic states, such as ferromagnetic and antiferromagnetic states. The latter method assumes that the magnetic coupling parameters remain constant regardless of the magnetic configuration. This can be regarded as an enforced modeling, as it assumes that the energies of intermediate magnetic states follow the Heisenberg model without explicitly sampling them. On the other hand, the (SC)² method determines J_{ij} by sampling relevant magnetic configurations while verifying whether the Heisenberg model can accurately reproduce the energy dataset.

Although we focus on magnetic configurations near the ground state, the (SC)² method is also applicable to the Curie-Weiss paramagnetic state by setting $\theta_{\text{max}} = 180^\circ$. Such paramagnetic states have also been studied in the context of the KKR-Green's function method and the coherent potential approximation [5]. The results of these two methods for bcc Fe are presented in Sec. S9 of the Supplementary Information.

B. Comparison with the spin-spiral method

We briefly review the differences between the (SC)² method and the spin-spiral method, both of which are nonperturbative approaches. The spin-spiral method, based on the generalized Bloch's theorem [18], is another procedure for sampling magnetic configurations [11]. Subsequently, exchange coupling parameters J_{ij} are evaluated to reproduce the energies of sampled spin-spiral states. A major advantage of this method is that it requires only a minimal magnetic unit cell, thus keeping computational costs relatively low. There are, however, some shortcomings that do not exist in the (SC)² method. For example, the spin-spiral method ignores the disorder caused by the excitation of multiple spin wave modes and the impact of this disorder on the electronic state, which is inevitable at finite temperatures. Moreover, spin-orbit coupling cannot be incorporated alongside the spin-spiral method because it breaks the translational symmetries assumed in the generalized Bloch's theorem.

We also note the extendability of the (SC)² method. First,

the (SC)² method is not limited to evaluating the isotropic lowest-order cluster interaction J_{ij} . For instance, Antal and co-workers have evaluated tensor-formed exchange coupling parameters, fourth-order interaction parameters, and on-site anisotropy parameters for a Cr trimer on Au(111) surface while considering the spin-orbit coupling [15]. Second, the effect of lattice vibrations on exchange coupling parameters can also be calculated straightforwardly, as demonstrated in Ref. [17]. Notably, the direct modeling of atomic displacements due to lattice vibrations in a supercell is a feature not available in the spin-spiral method with a minimal cell. The current limitation of the (SC)² method compared to other methods is its higher computational cost and the difficulty in systematically improving spin models. However, we expect these issues can be overcome in future by combining the spin-cluster expansion [19] with the torque method which is utilizing a constraining magnetic field [11].

C. Relation between spin-cluster expansion

Spin-cluster expansion method [19] provides a general framework for constructing classical spin models. In this method, the energy of a spin model is expressed as

$$E(\{\hat{e}_i\}) = E_0 + \sum_{\alpha} \sum_l \sum_m J_{\alpha lm} \Phi_{\alpha lm}(\{\hat{e}_i\}), \quad (4)$$

where $J_{\alpha lm}$ is the cluster interaction coefficient and $\Phi_{\alpha lm}$ represents the cluster function regarding cluster set α defined as

$$\Phi_{\alpha lm}(\{\hat{e}_i\}) = \sum_{i \in \alpha} y_{l_1 m_1}(\hat{e}_1) \dots y_{l_M m_M}(\hat{e}_M), \quad (5)$$

where y_{lm} is the spherical harmonics with indices (l, m) . Note that y_{lm} is defined in terms of the conventional spherical harmonics Y_{lm} as

$$y_{lm} = \sqrt{4\pi} Y_{lm}. \quad (6)$$

In practical applications, the number of clusters must be finite. In this case, the parameter set $\{J_{\alpha lm}\}$ depends on the sampled magnetic configurations and the selected clusters. The dependence on the selection of clusters diminishes as the number of considered clusters increases; however, this comes at the cost of a more complex model. Therefore, as long as the sampled dataset (a set of magnetic configuration and corresponding energy) obtained from DFT are sufficiently reproduced, it would be better to construct a model that effectively renormalizes higher-order cluster interactions using only a small number of lower-order clusters. Note that this discussion applies more generally to series expansions and the corresponding function fitting.

The Heisenberg model in Eq. (2) is a special case of the spin-cluster expansion model. The inner product between two spins $(\hat{e}_i \cdot \hat{e}_j)$ in the Heisenberg model incorporated into the

spin-cluster expansion as follows:

$$\hat{e}_i \cdot \hat{e}_j = \frac{1}{3} \sum_{m=-1}^1 y_{1m}^*(\hat{e}_i) y_{1m}(\hat{e}_j). \quad (7)$$

This relationship is straightforwardly derived from the spherical harmonics addition theorem;

$$P_l(\hat{e}_i \cdot \hat{e}_j) = \frac{1}{2l+1} \sum_{m=-l}^l y_{lm}^*(\hat{e}_i) y_{lm}(\hat{e}_j), \quad (8)$$

where P_l denotes the l -th Legendre polynomial. Although the Heisenberg model corresponds to the lowest-order cluster interactions within the spin-cluster expansion framework, higher-order interactions are renormalized into the J_{ij} parameters in Eq. (2) through the fitting procedure in Eq. (3). Therefore, the J_{ij} parameters naturally depend on the sampled magnetic configurations, as the magnitude of renormalization is strongly influenced by the choice of dataset. In fact, as discussed later in Sec. IV C, this dependence is one of the key points of this study.

The validity of the renormalization should be carefully justified by assessing whether the Heisenberg model sufficiently reproduces the DFT energies. If it does not, higher-order cluster interactions should be explicitly incorporated into the spin model. To address this point, in Sec. S8 of the Supplementary Information, we compare the energies calculated using DFT and the Heisenberg model for the systems examined in this study.

III. COMPUTATIONAL CONDITIONS

A. DFT calculations in the (SC)² method

In the (SC)² method, we employed constrained noncollinear spin DFT within the projector augmented-wave method [20] as implemented in the VASP package [21, 22]. The constrained local moment approach was employed to fix the direction of the atomic magnetic moments, while the magnitudes of the magnetic moments were allowed to relax. As the exchange-correlation functional, we used two generalized gradient approximations: PBEsol [23] for SrMnO₃, and PBE [24] for neodymium-magnet compounds and elemental 3d transition metals. These choices were made to facilitate comparisons with previous studies [12, 14]. The energy convergence criterion was set to 10⁻⁷ eV/atom. The spin-orbit coupling was not incorporated throughout this study. Other system-dependent conditions are described separately below.

We discuss the validity of relaxing the magnitudes of the magnetic moments. While classical spin models, including Eqs. (2) and (4), focus solely on the degrees of freedom associated with the spin orientations, this does not necessarily imply that the magnitudes of the magnetic moments remain fixed in DFT calculations. Rather, the contributions of longitudinal variations in magnetic moments are renormalized into the J_{ij} parameters through the regression procedure in Eq. (3).

Therefore, relaxing the magnitudes of the magnetic moments is appropriate as long as the contribution of longitudinal spin fluctuations remains insignificant.

1. SrMnO_3 with the type-G antiferromagnetic state

The plane-wave cutoff was set to 680 eV, and a k -grid spacing of approximately 0.17 \AA^{-1} in each reciprocal vector was used. To incorporate on-site Coulomb interactions, we applied the DFT+ U method [25] using $U_{\text{eff}} = 3.0 \text{ eV}$ [12]. We used two lattice constants following Ref. [12], specifically $a/a_{\text{eq}} = 1.0$ and 1.05 , where the equilibrium lattice constant $a_{\text{eq}} = 3.79 \text{ \AA}$ was adopted. A $2 \times 2 \times 2$ cubic cell (containing 40 atoms) was used. The radii of the atomic spheres, to which the constrained magnetic field was applied (VASP parameter RWIGS), were set to 2.0 \AA for Sr, 1.2 \AA for Mn, and 0.7 \AA for O.

2. $\text{Nd}_2\text{Fe}_{14}\text{B}$ and $\text{Nd}_2\text{Co}_{14}\text{B}$

The plane-wave cutoff was set to 350 eV, and a k -grid spacing of approximately 0.18 \AA^{-1} in each reciprocal vector was used. Lattice constants were set to experimental values [26, 27], whereas internal atomic coordinates are optimized. The radii of the atomic spheres for the constrained magnetic field were set as 1.5 \AA for Nd, 1.2 \AA for Fe and Co, 0.8 \AA for B. We used $1 \times 1 \times 1$ unit cell (containing 68 atoms). Although this relatively small unit cell introduces large size effect in the evaluation of J_{ij} itself, it does not pose major issues for the evaluation of T_C using the mean-field approximation [28] employed later. The size effect causes interactions with distant equivalent atomic pairs to be incorporated into the J_{ij} of nearby pairs. However, since the mean-field approximation eventually sums all J_{ij} between equivalent pairs, the size effect does not pose a problem for the evaluation of T_C .

3. Elemental $3d$ transition metals with bcc and fcc structures

The plane-wave cutoff was set to 350 eV, and a k -grid spacing of approximately 0.18 \AA^{-1} in each reciprocal vector was used. We used $4 \times 4 \times 4$ cubic supercells for bcc and $3 \times 3 \times 3$ cubic supercells for fcc. The radii of the atomic spheres were set to half the nearest neighbor distance in each system. The dependence of J_{ij} on the radii of the atomic spheres and the convergence with respect to the supercell size were summarized in Secs. S4 and S5 of the Supplementary Information. The lattice constants, reference magnetic configurations, and magnetic moments within an atomic site are provided in Table. I. Note the following two points: For bcc Cr, the reference magnetic state was assumed to be the type-I antiferromagnetic state in our calculations, although a spin-density wave is observed in experiments; for fcc Mn, we adopted a relatively large lattice constant (3.86 \AA) to be a ferromagnetic state, because this system exhibits a nonmagnetic state in a wide range of volumes around the equilibrium point.

TABLE I. Lattice constants (a), reference magnetic configurations, and the magnitude of magnetic moment $|m|$ per atomic site of elemental $3d$ transition metals. The notations AFM and FM denote antiferromagnetic and ferromagnetic, respectively. Lattice constants were obtained using structure optimization, except for fcc Mn (see the main text).

System	a (\AA)	Reference magnetic configuration	$ m $ (μ_B)
bcc			
Cr	2.85	Type-I AFM	1.04
Mn	2.79	FM	0.89
Fe	2.83	FM	2.21
Co	2.80	FM	1.81
Ni	2.80	FM	0.59
fcc			
Mn	3.86	FM	2.98
Fe	3.64	FM	2.60
Co	3.51	FM	1.65
Ni	3.52	FM	0.62

B. MFT-based method

The family of MFT-based methods has been implemented using various basis sets and DFT packages. To minimize the dependence on basis sets, we adopted tight-binding models with Wannier functions constructed from the same VASP package [21, 22] in the case of the (SC)² method. The Wannier functions were generated using the Wannier90 package [29], and the TB2J package [9] was subsequently employed to evaluate J_{ij} . For the results concerning elemental $3d$ transition metals, we also present J_{ij} values obtained with three different upper bounds of integration with respect to band energy: $\varepsilon_F - 0.1 \text{ eV}$, ε_F , and $\varepsilon_F + 0.1 \text{ eV}$ (Please see Ref. [6, 9] for details and definitions). This approach was taken to determine whether the differences between the conventional MFT-based method and the (SC)² method are attributable to sensitivity to the integration limits. Section S6 of the Supplementary Information presents a comparison of band dispersions obtained from the tight-binding model using Wannier functions and those calculated from DFT.

Unfortunately, in the case of neodymium-magnet compounds, the evaluations of J_{ij} via constructing Wannier functions are very computationally demanding. We therefore employed the KKR-Green's function method within the muffin-tin approximation implemented in AkaiKKR package [30]. The $4f$ electrons in the Nd atoms were treated as core electrons (open-core approximation). The maximum angular momentum of partial waves for all elements was set to 2. The same structural parameters used in the (SC)² method were applied in all cases. To verify the converged electronic states obtained from both packages (VASP and AkaiKKR) are sufficiently consistent, we compared the magnetic moments of all sites, as summarized in Sec. S2 of the Supplementary Information.

C. Classical Monte Carlo simulations

Classical Monte Carlo simulations, implemented in the EspinS package [31], were carried out to numerically evaluate the magnetic phase transition temperatures of elemental $3d$ transition metals. Interaction shells up to the 10th nearest neighbor for bcc structures and the 7th nearest neighbor for fcc structures were considered for J_{ij} . The results of the (SC)² method were calculated using J_{ij} in $4 \times 4 \times 4$ supercell for bcc and $3 \times 3 \times 3$ supercell for fcc. For both structures, $16 \times 16 \times 16$ sites were adopted, with 300,000 steps for equilibration and 2,000,000 steps for sampling. The magnetic phase transition temperatures were defined as the temperature at which the specific heat exhibits a peak.

IV. RESULTS

A. SrMnO₃ with the type-G antiferromagnetic state

Perovskite SrMnO₃ exhibits multiferroicity [32] and has therefore attracted a lot of interest for new information technologies. In addition, the strong dependence of J_{ij} between Mn atoms on strain, which induces magnetic phase transitions, was experimentally examined [33]. Thus, the quantitative evaluation of J_{ij} is crucial for reliable materials and device design with sensitive magnetic properties. A recent study, however, demonstrated that the J_{ij} of SrMnO₃ obtained from the MFT is qualitatively different from the results of self-consistent calculations [12]; under isotropic volume expansion, the MFT-based method predicted a negative first-nearest exchange coupling parameter J_{01} in the type-G antiferromagnetic state, but it appears to be positive according to self-consistent calculations. Here, we reexamine their results and discuss the origin of the difference in J_{01} in terms of $\mathcal{O}(\delta n^2, \delta m^2)$ in Eq. (1).

Figure 1 shows J_{01} between Mn atoms in cubic SrMnO₃ for different lattice constants $a/a_{\text{eq}} = 1.0$ and 1.05 (the J_{ij} values for more distant atomic pairs are summarized in Sec. S1 of the Supplementary Information). In addition to the results from the MFT-based and the (SC)² methods, we also present results from a total energy method, where J_{01} is approximated from the energy difference between the type-G antiferromagnetic and ferromagnetic states as follows:

$$J_{01} = \frac{E_{\text{total}}^{\text{AFM}} - E_{\text{total}}^{\text{FM}}}{N}, \quad (9)$$

where N ($= 6$ in this case) is the number of equivalent Mn-Mn bonds at the first-nearest neighbor, $E_{\text{total}}^{\text{AFM}}$ and $E_{\text{total}}^{\text{FM}}$ are the total energies of the type-G antiferromagnetic and ferromagnetic states per formula unit, respectively. This total energy method makes it easy to see the relative energy difference between the two magnetic states (note that J_{ij} at the second-nearest neighbor and beyond are sufficiently small relative to the one at the first-nearest neighbor). As reported in Ref. [12], the MFT gives negative J_{01} (favoring antiferromagnetic coupling) for both lattice constants. However, the result of total energy method indicates J_{01} for $a/a_{\text{eq}} = 1.05$ is positive. On the

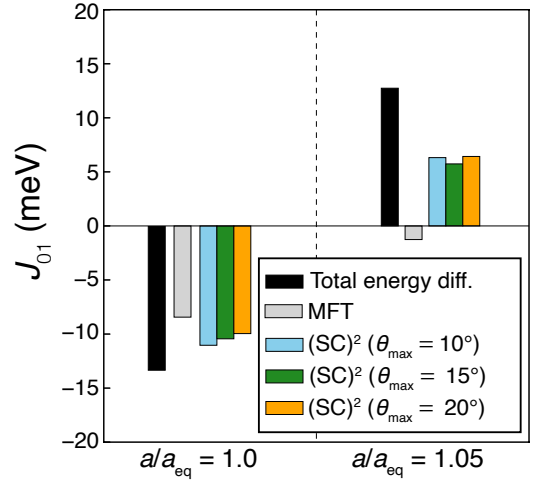


FIG. 1. Exchange coupling parameters at the first-nearest neighbor Mn-Mn pair J_{01} in cubic SrMnO₃ with the type-G antiferromagnetic state. The black and gray bars represent the results obtained from the total energy method in Eq. (9) and the MFT-based method, respectively. The other colored bars show the results from the (SC)² method with three difference upper bounds for the polar angle θ : 10° (blue), 15° (green), and 20° (orange). The lattice constants were set to $a/a_{\text{eq}} = 1.0$ and 1.05, where $a_{\text{eq}} = 3.79 \text{ \AA}$.

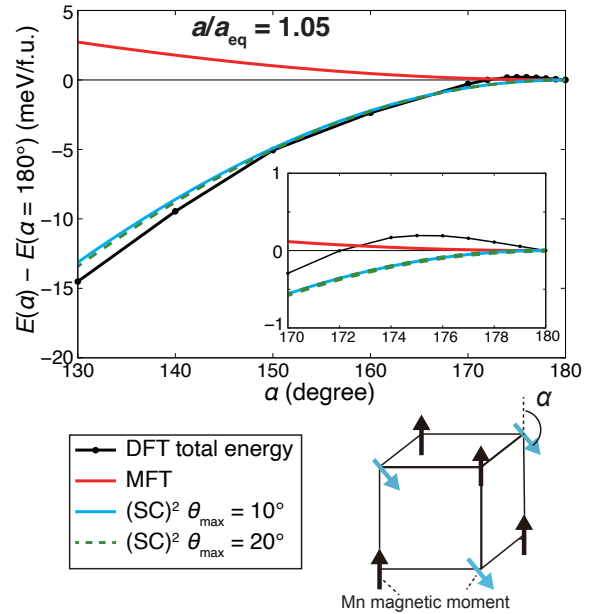


FIG. 2. Total energy variation (per formula unit) for the lattice constant $a/a_{\text{eq}} = 1.05$ as a function of the rotation angle α of Mn magnetic moments, illustrated in the lower right. The type-G antiferromagnetic state corresponds to $\alpha = 180^\circ$. The black line represents DFT total energy. The blue, dashed green, and red lines depict the energy variations using Eq. (10) with J_{ij} obtained from the (SC)² method for $\theta_{\text{max}} = 10^\circ$, $\theta_{\text{max}} = 20^\circ$, and the MFT-based method, respectively. The inset shows a magnified view of the energy variations in the range between 170° and 180° .

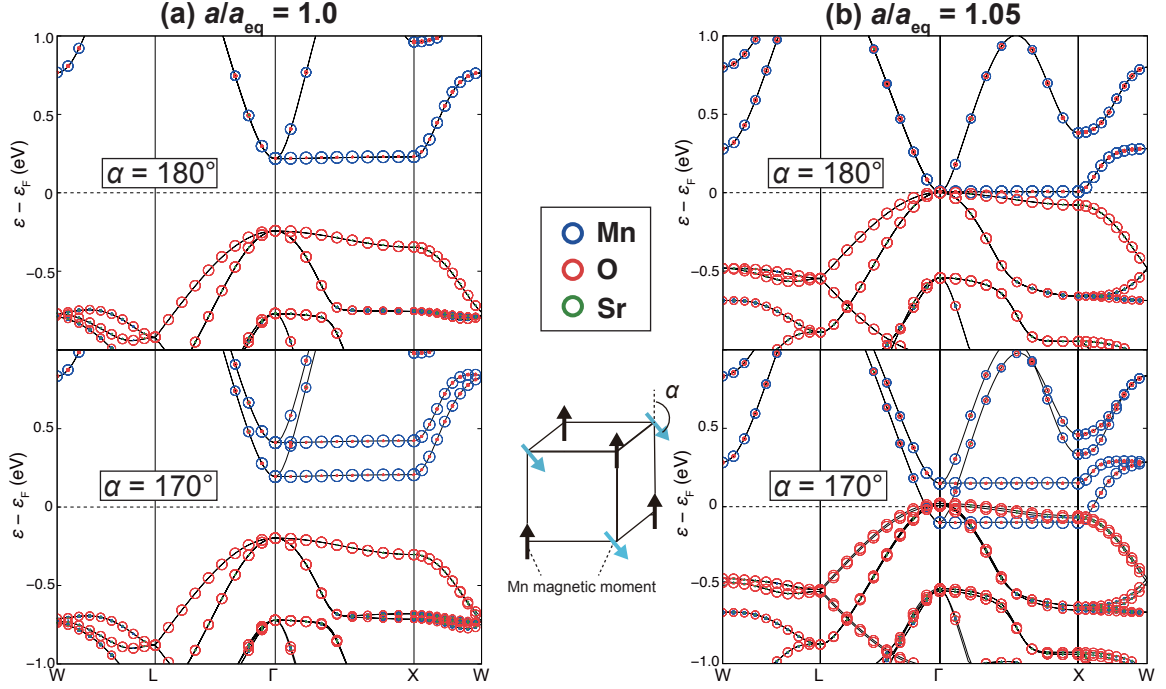


FIG. 3. Element-decomposed band dispersions of SrMnO₃ with and without rotation of Mn magnetic moments, as illustrated in the inset. Panel (a) corresponds to the equilibrium lattice constant $a/a_{\text{eq}} = 1.0$, whereas panel (b) corresponds to $a/a_{\text{eq}} = 1.05$. The blue, red, and green circles denote the contributions from Mn, O, and Sr, respectively. The band dispersions and the element contributions were plotted by using VASPKIT [34].

other hand, the (SC)² method correctly reproduced the change in the sign of J_{01} with volume expansion.

To investigate the differences between the MFT-based method and the (SC)² method, we calculated the total energy variation as a function of the rotation angle α of Mn magnetic moments, as shown in Fig. 2, following Ref. [12]. The rotation angle is taken to continuously varied from the type-G antiferromagnetic state to the ferromagnetic state. The Heisenberg models derived from the MFT-based method and the (SC)² method also yield energy variations per formula unit as a function of α [12]:

$$E(\alpha) = -\frac{1}{N_{\text{Mn}}} \sum_{ij} J_{ij} \hat{e}_i \cdot \hat{e}_j \quad (10)$$

$$= -(6J_{01} + 8J_{03}) \cos \alpha,$$

where $N_{\text{Mn}} (= 2$ in this case) is the number of Mn atoms, and J_{03} is the third-nearest exchange coupling parameter (although its magnitude is negligible in both methods, as shown in Ref. [12] and Sec. S1 of the Supplementary Information). The results of (SC)² method correctly reproduced the total energy variation in the range from a rotation angle 180° (the type-G antiferromagnetic state) to 140°. In contrast, the MFT-based method failed to capture the energy variation in this range, as already reported in Ref. [12]. However, as shown in the inset of Fig. 2, the MFT-based method qualitatively captures the stability of the magnetic state correctly in the immediate vicinity of 180°. In other words, the sign of the curvature of the energy landscape at 180° is consistent.

To examine the origin of the peculiar local minimum at $\alpha = 180^\circ$, we focus on the underlying electronic structure. Figures 3 (a) and (b) show the element-decomposed band dispersions of SrMnO₃ with and without the rotation of Mn magnetic moments ($\alpha = 170^\circ$ and 180°), respectively. For $a/a_{\text{eq}} = 1.0$, the band gap remains open, regardless of the magnetic moment rotation (Fig. 3 (a)). In contrast, for $a/a_{\text{eq}} = 1.05$, the band gap closes, and flat bands consisting of Mn and O states appear near the Fermi level along the $\Gamma - X$ line (upper panel of Fig. 3 (b)). Upon rotating magnetic moments, the degenerate Mn bands split into occupied and unoccupied states, while the occupied O bands near the Γ point shift into unoccupied state (lower panel of Fig. 3 (b)). Consequently, the changes in electron density associated with the rotation of Mn magnetic moments differ significantly before and after the volumetric expansion. Figure 4 shows the charge density differences $\Delta n(\mathbf{r})$ resulting from the rotation of Mn magnetic moments for $a/a_{\text{eq}} = 1.0$ and 1.05, defined as

$$\Delta n(\mathbf{r}) = n^{\alpha=170^\circ}(\mathbf{r}) - n^{\alpha=180^\circ}(\mathbf{r}), \quad (11)$$

where $n^{\alpha=\theta}(\mathbf{r})$ represents the electron density at position \mathbf{r} when magnetic moments are rotated by an angle θ . In the case of $a/a_{\text{eq}} = 1.05$ (Fig. 4 (a)), we can see a large charge density difference at the Mn and O sites compared with the case of $a/a_{\text{eq}} = 1.0$ (Fig. 4 (a)), due to the change in the orbital occupations described above. These behaviors of charge density difference are directly related to the magnitude of the contribution of $\mathcal{O}(\delta n^2, \delta m^2)$ in Eq. (1).

Although the MFT-based method appears to yield an inconsistent result, it would be a correct result for the infinitesimal rotation angle. As shown in Fig. 2 (b) in Ref. [12], the energy landscape around the antiferromagnetic state at $a/a_{\text{eq}} = 1.05$ has somewhat complex shape; we expect that the complexity is also related to the change in the orbital occupations. Therefore, the MFT-based method would be valid in the infinitesimal rotation range where the change in the orbital occupations can be neglected. However, when the effective range of rotation angles for the MFT-based method is extremely narrow, a non-perturbative method would be more practical for constructing an effective spin model.

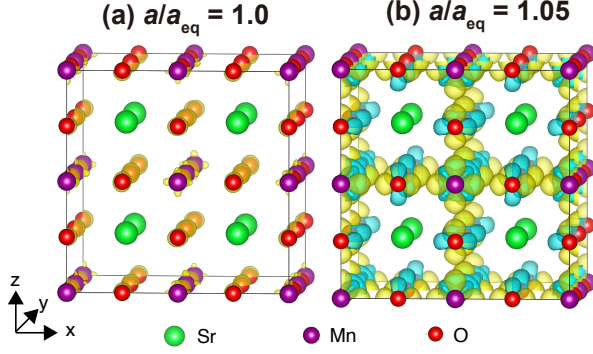


FIG. 4. Charge density differences $\Delta n(\mathbf{r})$ in SrMnO_3 as defined in Eq. (11) between rotation angles $\alpha = 170^\circ$ and $\alpha = 180^\circ$, drawn using VESTA software [35]. Panel (a) corresponds to the equilibrium lattice constant $a/a_{\text{eq}} = 1.0$, whereas panel (b) corresponds to $a/a_{\text{eq}} = 1.05$. The isosurface levels represented in yellow and blue are set to $+2 \times 10^{-5}$ and -2×10^{-5} bohr $^{-3}$, respectively.

B. $\text{Nd}_2\text{Fe}_{14}\text{B}$ and $\text{Nd}_2\text{Co}_{14}\text{B}$

Evaluation of J_{ij} plays an important role in the materials design of magnet compounds, because the stronger exchange couplings suppress demagnetization due to temperature, i.e., larger J_{ij} values lead to higher T_C . Nevertheless, previous methods based on the MFT for evaluating T_C through J_{ij} of magnet compounds have been unsatisfactory in terms of quantitative evaluation; the MFT-based method failed to reproduce the increase in T_C when Co was substituted with Fe in $\text{Nd}_2\text{Fe}_{14}\text{B}$ [14]. Magnetic interactions are important not only for understanding existing permanent magnets [36, 37] but also for exploring new magnetic compounds [38]. This problem, therefore, must be resolved for the reliable materials design of magnet compounds.

Figure 5 shows the differences between T_C values of $\text{Nd}_2\text{Fe}_{14}\text{B}$ and $\text{Nd}_2\text{Co}_{14}\text{B}$. Note that the ferromagnetic ground state is assumed as a reference state in both the MFT-based method and the $(\text{SC})^2$ method. As reported in Ref. [14], the MFT-based method cannot reproduce the increase in T_C when Fe is substituted with Co. Although this disagreement with experimental results can also be observed in the results from the $(\text{SC})^2$ method for $\theta_{\text{max}} = 10^\circ$, a correct trend is obtained with

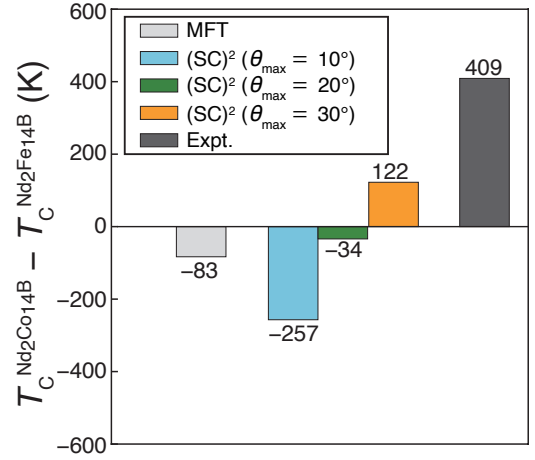


FIG. 5. Differences in the T_C of $\text{Nd}_2\text{Co}_{14}\text{B}$ and $\text{Nd}_2\text{Fe}_{14}\text{B}$. The gray and black bars represent values obtained using the MFT-based method and experiments, respectively. The blue, green, and orange bars indicate values obtained using the $(\text{SC})^2$ method, with the upper bound of θ set to 10° , 20° , and 30° , respectively. Theoretical values are obtained using the mean-field approximation. Experimental values were taken from Ref. [39, 40].

increasing θ_{max} ; T_C of $\text{Nd}_2\text{Co}_{14}\text{B}$ becomes larger than that of $\text{Nd}_2\text{Fe}_{14}\text{B}$ when $\theta_{\text{max}} = 30^\circ$. This is because the decrease in T_C due to magnetic disordering is greater for $\text{Nd}_2\text{Fe}_{14}\text{B}$ than for $\text{Nd}_2\text{Co}_{14}\text{B}$ (absolute values of T_C are summarized in Sec. S3 in the Supplementary Information). This angular dependence of T_C (or J_{ij}) arises due to the renormalization of higher-order cluster interactions beyond the Heisenberg model into J_{ij} . In Sec. IV C, we will show that these renormalized higher-order cluster interactions do not primarily originate from the $\delta^* E_{\text{band}}$ term in Eq. (1), which can be accounted for in MFT-based methods. Instead, they mainly stem from the $\mathcal{O}(\delta n^2, \delta m^2)$ contribution, which can only be captured by nonperturbative methods.

More quantitative evaluations, including other temperature effects, are needed to conclude the cause of the disagreement in T_C between theory and experiments. For example, $\text{Nd}_2\text{Fe}_{14}\text{B}$ is reported to exhibit strong magnetism-dependent phonons [41], which are shifts of phonon frequencies due to magnetic disordering. As we previously pointed out in Ref. [42], the magnetism-dependent phonons affect the determination of equilibrium magnetic states, and resulting in changes in the theoretical T_C . In addition, the direct impact of lattice vibrations on J_{ij} would affect T_C [17]. Although further investigation incorporating additional temperature effects is necessary, our results clearly demonstrate the importance of nonperturbative methods in capturing the concentration dependence of T_C in the $\text{Nd}_2(\text{Fe}, \text{Co})_{14}\text{B}$ system.

C. Elemental 3d transition metals with bcc and fcc structures

Figures 6 (a)-(e) and 7 (a)-(d) show the J_{ij} values for 3d transition metals with bcc and fcc structures, respectively. Generally, J_{ij} values beyond the second nearest neighbor exhibit

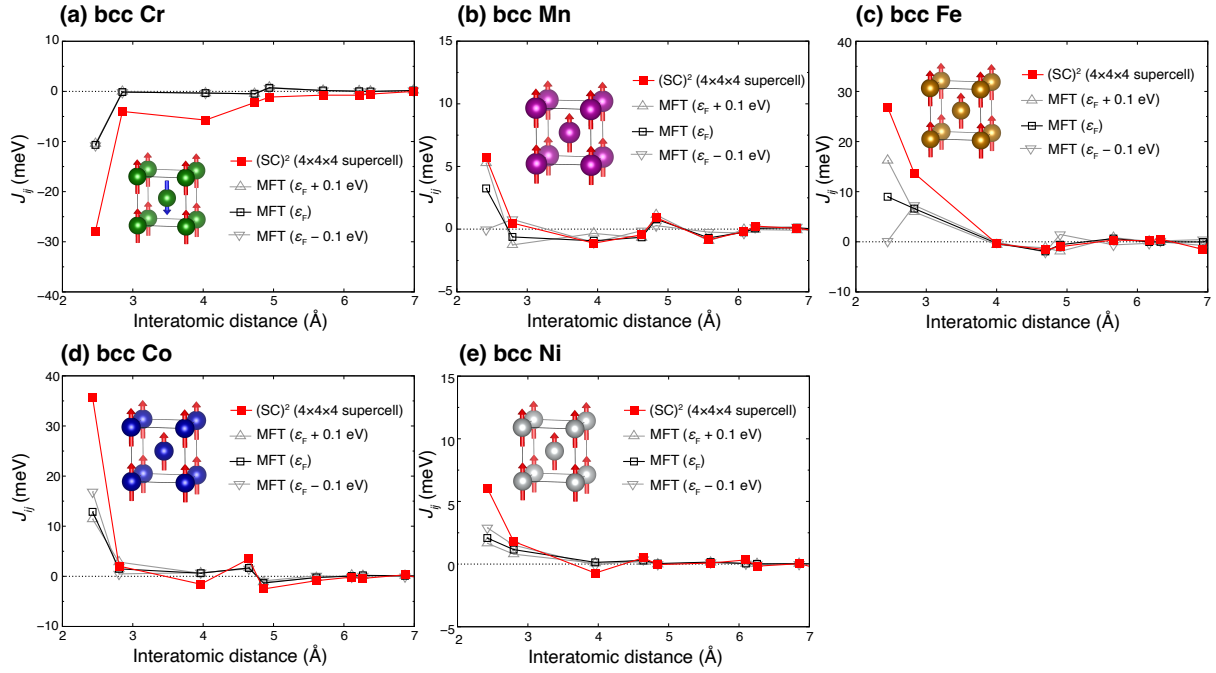


FIG. 6. Exchange coupling parameters J_{ij} in (a) bcc Cr, (b) bcc Mn, (c) bcc Fe, (d) bcc Co, and (e) bcc Ni. The results of the $(SC)^2$ method were obtained using $\theta_{\max} = 10^\circ$. In the $(SC)^2$ method, a $4 \times 4 \times 4$ body-centered-cubic supercell containing 128 atoms was used. In the MFT-based method, we present results for three different upper bound of integration with respect to band energy: $\epsilon_F - 0.1$ eV, ϵ_F , and $\epsilon_F + 0.1$ eV. The reference magnetic state in each system is also shown using VESTA software [35].

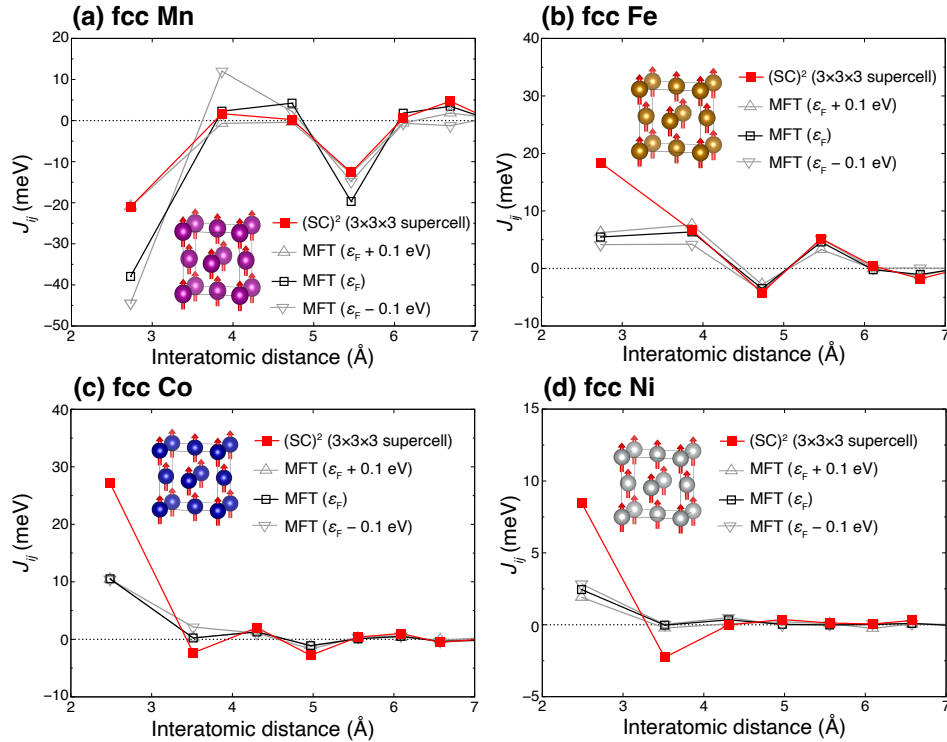


FIG. 7. Exchange coupling parameters J_{ij} in (a) fcc Mn, (b) fcc Fe, (c) fcc Co, and (d) fcc Ni. The results of the $(SC)^2$ method were obtained using $\theta_{\max} = 10^\circ$. In the $(SC)^2$ method, a $3 \times 3 \times 3$ face-centered-cubic supercell containing 108 atoms was used. In the MFT-based method, we present results for three different upper bound of integration with respect to band energy: $\epsilon_F - 0.1$ eV, ϵ_F , and $\epsilon_F + 0.1$ eV. The reference magnetic state in each system is also shown using VESTA software [35].

relatively good agreement between the two methods. However, significant differences in exchange coupling parameters at the first-nearest neighbors J_{01} are remarkable between the two methods in all of the systems. In particular, the differences in systems, except for bcc Mn and fcc Mn, cannot be attributed to the sensitivity to the integration limits with respect to band energy in the MFT-based method. We further investigate the origin of these large discrepancies in the following parts.

We calculated the change in J_{01} as the maximum rotation angle θ_{\max} was varied from 10° to 20° , as shown in Fig. 8. Systems with a large difference in J_{ij} between the (SC)² method and the MFT-based method tend to also have a large angular dependence of J_{01} . As discussed in Sec. II C, the angular dependence of J_{01} (i.e., the dependence on the sampled magnetic configurations) results from the renormalization of higher-order cluster interactions beyond the Heisenberg model. Here, we demonstrate the origin of the angular dependence of J_{ij} using the biquadratic interaction $(-B_{ij}(\hat{e}_i \cdot \hat{e}_j)^2)$ as a representative of higher-order cluster interactions. The spin hamiltonian is

$$\mathcal{H} = -J_{ij}\hat{e}_i \cdot \hat{e}_j - B_{ij}(\hat{e}_i \cdot \hat{e}_j)^2. \quad (12)$$

Energy as a function of θ_{\max} becomes

$$E = -J_{ij}\langle\hat{e}_i \cdot \hat{e}_j\rangle_{\theta_{\max}} - B_{ij}\langle(\hat{e}_i \cdot \hat{e}_j)^2\rangle_{\theta_{\max}}, \quad (13)$$

where $\langle\cdots\rangle_{\theta_{\max}}$ denotes an expectation value when the upper bound of θ is θ_{\max} . The angular dependent J_{ij} , expressed as $J_{ij}(\theta_{\max})$, arises when the biquadratic term is renormalized as

$$\begin{aligned} & -J_{ij}\langle\hat{e}_i \cdot \hat{e}_j\rangle_{\theta_{\max}} - B_{ij}\langle(\hat{e}_i \cdot \hat{e}_j)^2\rangle_{\theta_{\max}} \\ = & -\left(J_{ij} + B_{ij}\frac{\langle(\hat{e}_i \cdot \hat{e}_j)^2\rangle_{\theta_{\max}}}{\langle\hat{e}_i \cdot \hat{e}_j\rangle_{\theta_{\max}}}\right)\langle\hat{e}_i \cdot \hat{e}_j\rangle_{\theta_{\max}} \quad (14) \\ = & -J_{ij}(\theta_{\max})\langle\hat{e}_i \cdot \hat{e}_j\rangle_{\theta_{\max}}, \end{aligned}$$

where

$$J_{ij}(\theta_{\max}) = J_{ij} + B_{ij}\frac{\langle(\hat{e}_i \cdot \hat{e}_j)^2\rangle_{\theta_{\max}}}{\langle\hat{e}_i \cdot \hat{e}_j\rangle_{\theta_{\max}}}, \quad (15)$$

$$\begin{aligned} \frac{\langle(\hat{e}_i \cdot \hat{e}_j)^2\rangle_{\theta_{\max}}}{\langle\hat{e}_i \cdot \hat{e}_j\rangle_{\theta_{\max}}} &= \frac{2}{\sin^4\theta_{\max}} \\ &\times \left[\left(-\frac{3}{4}\cos\theta_{\max} + \frac{1}{12}\cos 3\theta_{\max} + \frac{2}{3} \right)^2 \right. \\ &\left. + \frac{2}{9}(1 - \cos^3\theta_{\max})^2 \right]. \quad (16) \end{aligned}$$

The derivation of $\langle(\hat{e}_i \cdot \hat{e}_j)^2\rangle_{\theta_{\max}}/\langle\hat{e}_i \cdot \hat{e}_j\rangle_{\theta_{\max}}$ is described in Sec. S7 of the Supplementary Information. The biquadratic interaction can also be evaluated within the MFT. However, the typical values of the $|B_{ij}|$ obtained from the MFT-based method (~ 5 meV for bcc Fe, ≤ 0.1 meV for hcp Co and fcc Ni [43]) cannot completely explain the large angular dependence of $J_{ij}(\theta_{\max})$; if the change in $|J_{ij}(\theta_{\max})|$ when θ_{\max} increases

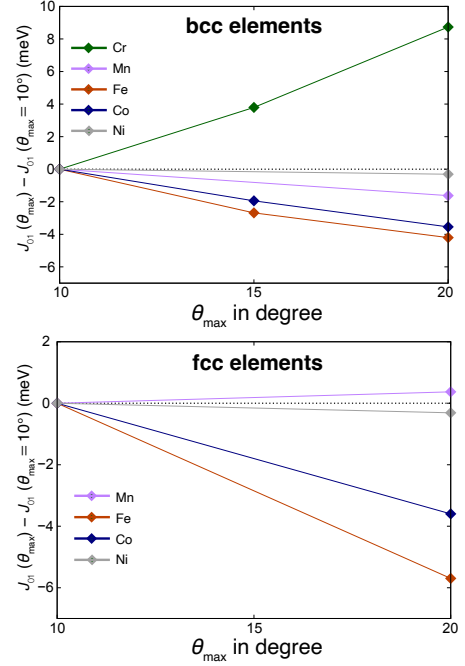


FIG. 8. Dependence of J_{01} on θ_{\max} for elemental 3d transition metals. The vertical axis represents the deviation of J_{01} from its value at $\theta_{\max} = 10^\circ$.

from 10° to 20° is 1 meV, $|B_{ij}|$ becomes 24 meV. It is also unlikely that other higher-order cluster interactions derived from MFT-based methods are the cause of the angular dependence [43]. MFT-based methods evaluate magnetic interactions, including J_{ij} and B_{ij} , by neglecting $\mathcal{O}(\delta n^2, \delta m^2)$ contributions and considering only $\delta^* E_{\text{band}}$ in principle. Therefore, the large angular dependence of J_{ij} obtained from the (SC)² method suggests that $\mathcal{O}(\delta n^2, \delta m^2)$ contributions are essential for the quantitative evaluation of magnetic interactions, even for relatively small spin rotation angles such as $\theta_{\max} = 10^\circ$.

We comment on the relatively large difference in J_{01} between the (SC)² method and the MFT, despite the small angular dependence of J_{01} for bcc Ni (Fig. 6 (e)) and fcc Ni (Fig. 7 (d)). The cause of the difference might be the long-wavelength approximation in the MFT, which is less accurate for the evaluation of J_{ij} in strong itinerant magnetic materials as discussed in Ref. [44]; $J_{01} = 8.3$ meV in fcc Ni, obtained by going beyond the long-wavelength approximation [44], is consistent with the value obtained using the (SC)² method (Fig. 7 (d)). Such differences in the implementation of MFT-based methods may be related to the fact that the J_{ij} parameters obtained via the (SC)² method do not align with those from MFT-based methods in the limit as $\theta_{\max} \rightarrow 0^\circ$. In fact, MFT-based methods yield J_{ij} values that exhibit variations due to differences in basis sets and specific implementation details [4, 10]. Furthermore, magnetic configurations with θ_{\max} ranging from 10° to 20° already lie outside of the regime where MFT is valid, as suggested by the large angular dependence of J_{ij} observed in $\text{Nd}_2\text{Fe}_{14}\text{B}$, $\text{Nd}_2\text{Co}_{14}\text{B}$, and 3d transition metals; it appears that the orbital occupations near the Fermi surface in met-

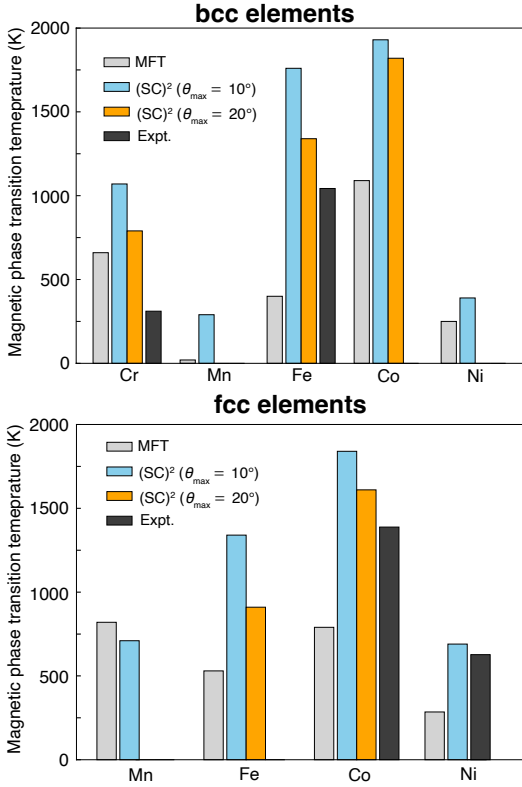


FIG. 9. Magnetic phase transition temperatures of elemental $3d$ metals obtained using the classical Monte Carlo simulations. For the systems that exhibit a large angular dependence of J_{01} in Fig. 8, the results for $\theta_{\max} = 20^\circ$ are also shown. Experimental values are also arranged for comparison [45]. The results obtained using the MFT-based method are based on J_{ij} values calculated with the upper limit of the band energy set to ε_F . Note that the experimental value of bcc Cr is the one for the antiferromagnetic spin-density wave state [46] whereas calculated values here are those for the type-I antiferromagnetic state as illustrated in Fig. 6 (a).

als can change as the spins rotate, potentially contributing as $\mathcal{O}(\delta n^2, \delta m^2)$ to the energy variation. Consequently, a naive extrapolation to $\theta_{\max} = 0^\circ$ would lead to different J_{ij} values from MFT-based methods.

We also evaluated the magnetic phase transition temperatures by using classical Monte Carlo simulations, as shown in Fig. 9 with some experimental values. Reflecting the larger $|J_{01}|$, magnetic phase transition temperatures by the $(\text{SC})^2$ method are larger than those obtained using the MFT, except for fcc Mn. Although magnetic phase transition temperatures by the $(\text{SC})^2$ method seem to overestimate experimental values, the discrepancies will probably be lowered by considering further temperature effects, such as lattice vibrations [17] and the stabilization of paramagnetic states by magnetism-dependent phonons [42, 47], already described in Sec. IV B. Therefore, the tendency to overestimate T_C when lattice vibration effects are neglected reflects a correct trend and further validates the nonperturbative method.

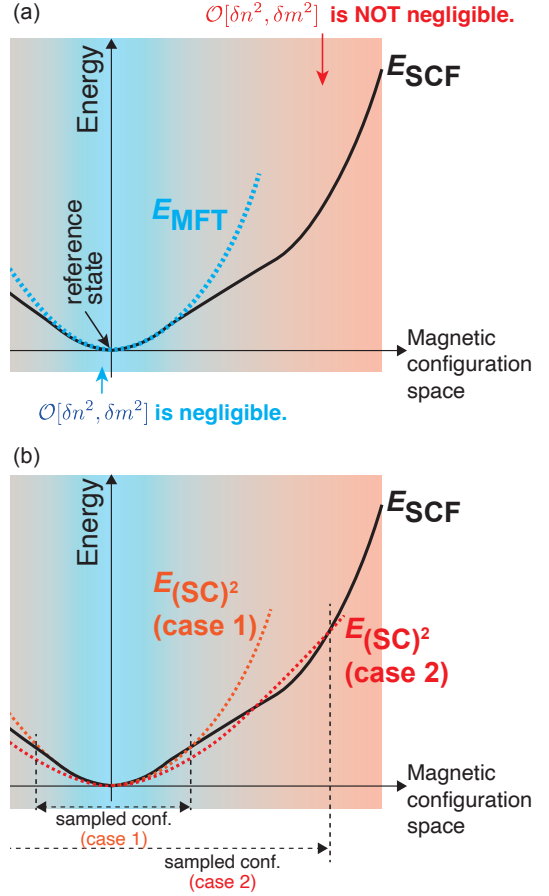


FIG. 10. Schematic representation of the energy landscape as a function of magnetic configuration around a reference magnetic state. Black lines represent the energy obtained from self-consistent calculations (E_{SCF}). The blue line in (a) represents the energy variation using J_{ij} evaluated by the MFT-based method (E_{MFT}). The orange and red lines in (b) correspond to the energy variation using J_{ij} evaluated by the $(\text{SC})^2$ method ($E_{(\text{SC})^2}$) for different sampled magnetic configurations. MFT-based methods can only reproduce the energy within the range where $\mathcal{O}(\delta n^2, \delta m^2)$ is negligible (indicated by the blue area). In contrast, the $(\text{SC})^2$ method constructs an effective model that reproduces the energy variation depending on the sampled magnetic configurations by considering not only $\delta^* E_{\text{band}}$ but also $\mathcal{O}(\delta n^2, \delta m^2)$.

V. DISCUSSION

We have recognized the critical role of $\mathcal{O}(\delta n^2, \delta m^2)$ contributions for the quantitative evaluation of magnetic interactions throughout this study. This finding suggests that, particularly for metallic systems, the range of rotation angles where MFT remains valid is narrower than previously assumed. To illustrate this point, Figure 10 presents a schematic representation of the energy landscape as a function of magnetic configuration around a reference magnetic state. The blue area in Fig 10 (a) represents the range where $\mathcal{O}(\delta n^2, \delta m^2)$ can be neglected to reproduce the self-consistent energy (E_{SCF} indicated by the black line). It is important to recognize that,

regardless of how much MFT-based methods are refined or extended to account for higher-order cluster interactions, they are fundamentally limited to reproducing only the region indicated in blue, as shown by the blue dashed line in Fig. 10 (a). Beyond this range, there inevitably exists a region in which $\mathcal{O}(\delta n^2, \delta m^2)$ must be considered to quantitatively reproduce E_{SCF} . In this region, E_{SCF} may exhibit complex variations due to the contributions of $\mathcal{O}(\delta n^2, \delta m^2)$, as demonstrated in SrMnO₃ at $a/a_0 = 1.05$. Even under such conditions, the Heisenberg model remains applicable as a phenomenological model as long as it sufficiently reproduces E_{SCF} . However, the J_{ij} parameters depend on the sampled magnetic configurations due to variations in the magnitude of the renormalization of $\mathcal{O}(\delta n^2, \delta m^2)$ contributions as illustrated by $E_{(\text{SC})^2}$ in case 1 and case 2 of Fig. 10 (b).

VI. CONCLUSION

We have demonstrated the discrepancies between perturbative and nonperturbative methods for calculating exchange coupling parameters in various magnetic materials. For SrMnO₃ with the type-G antiferromagnetic state, the nonperturbative method reproduced the correct sign of J_{ij} under isotropic volume expansion, whereas the MFT-based method did not. Although the MFT-based methods may be valid for infinitesimal rotations, accounting for changes in orbital occupations and the resulting charge density differences is essential to construct an effective Heisenberg model at finite rotation angles. In the neodymium-magnet compounds, the nonperturbative method revealed that the large difference in the sensitivity of J_{ij} and resulting in T_C on magnetic disordering between Nd₂Fe₁₄B and Nd₂Fe₁₄B; Nd₂Fe₁₄B rapidly decreases in T_C with increasing magnetic disordering, while Nd₂Co₁₄B shows a much weaker dependence. This provides important insights for quantitative understanding of composition dependence of J_{ij} and T_C in magnet systems. For elemental 3d transition metals with bcc and fcc structures, the nonperturbative method shows large discrepancies in J_{ij} at

first-nearest neighbors compared to the MFT-based method. We discussed these discrepancies in terms of the angular dependence of J_{ij} and attributed them to the contribution of $\mathcal{O}(\delta n^2, \delta m^2)$ on energy variation.

MFT-based methods continue to evolve, with ongoing improvements in their accuracy and an expanding range of applications expected in the future. At the same time, it is important to recognize the theoretical limitations of MFT-based methods, as they are inherently based on perturbation theory. On the other hand, the nonperturbative method realizes more quantitiveness in the construction of effective spin models by renormalizing all of the contributions, including $\mathcal{O}(\delta n^2, \delta m^2)$. In the future, the complementary use of these two methods would be advantageous for both the quantitative and qualitative analysis of magnetic interactions. For example, in regions where the magnetic states are in good agreement with nonperturbative methods, perturbative methods can be used to decompose the interactions between orbitals [?]. We plan to further develop the nonperturbative method and release it to the community in a user-friendly format. This advancement is expected to enhance the reliability and accessibility of the analysis and design of magnetic materials.

ACKNOWLEDGMENTS

This work was partly supported by JSPS KAKENHI Grant Number JP24K01144 and MEXT-DXMag Grant Number JPMXP1122715503. The calculations were partly carried out by using facilities of the Supercomputer Center at the Institute for Solid State Physics, the University of Tokyo, and TSUB-AME4.0 supercomputer at Institute of Science Tokyo.

CONFLICT OF INTEREST

The authors declare no conflicts of interest.

-
- [1] Dey, P. & Roy, J. N. *Spintronics: Fundamentals and Applications* (Springer, Singapore, 2021). URL <https://link.springer.com/10.1007/978-981-16-0069-2>.
- [2] Eriksson, O., Bergman, A., Bergqvist, L. & Hellsvik, J. *Atomistic Spin Dynamics: Foundations and Applications* (Oxford University Press, 2016). URL <https://books.google.co.jp/books?id=89pJAQAACAAJ>.
- [3] Mankovsky, S. & Ebert, H. First-principles calculation of the parameters used by atomistic magnetic simulations. *Electronic Structure* **4**, 034004 (2022). URL <https://dx.doi.org/10.1088/2516-1075/ac89c3>. Publisher: IOP Publishing.
- [4] Szilva, A. et al. Quantitative theory of magnetic interactions in solids. *Reviews of Modern Physics* **95**, 035004 (2023). URL <https://link.aps.org/doi/10.1103/RevModPhys.95.035004>. Publisher: American Physical Society.
- [5] Oguchi, T., Terakura, K. & Hamada, N. Magnetism of iron above the Curie temperature. *Journal of Physics F: Metal Physics* **13**, 145 (1983). URL <https://dx.doi.org/10.1088/0305-4608/13/1/018>.
- [6] Liechtenstein, A. I., Katsnelson, M. I., Antropov, V. P. & Gubanov, V. A. Local spin density functional approach to the theory of exchange interactions in ferromagnetic metals and alloys. *Journal of Magnetism and Magnetic Materials* **67**, 65–74 (1987). URL <https://www.sciencedirect.com/science/article/pii/0304885387907219>.
- [7] Terasawa, A., Matsumoto, M., Ozaki, T. & Gohda, Y. Efficient Algorithm Based on Liechtenstein Method for Computing Exchange Coupling Constants Using Localized Basis Set. *Journal of the Physical Society of Japan* **88**, 114706

- (2019). URL <https://journals.jps.jp/doi/10.7566/JPSJ.88.114706>. Publisher: The Physical Society of Japan.
- [8] Nomoto, T., Koretsune, T. & Arita, R. Local force method for the ab initio tight-binding model: Effect of spin-dependent hopping on exchange interactions. *Physical Review B* **102**, 014444 (2020). URL <https://link.aps.org/doi/10.1103/PhysRevB.102.014444>. Publisher: American Physical Society.
- [9] He, X., Helbig, N., Verstraete, M. J. & Bousquet, E. TB2J: A python package for computing magnetic interaction parameters. *Computer Physics Communications* **264**, 107938 (2021). URL <https://www.sciencedirect.com/science/article/pii/S001046521000679>.
- [10] Solovyev, I. V. Exchange interactions and magnetic force theorem. *Physical Review B* **103**, 104428 (2021). URL <https://link.aps.org/doi/10.1103/PhysRevB.103.104428>. Publisher: American Physical Society.
- [11] Jacobsson, A. et al. Efficient parameterisation of non-collinear energy landscapes in itinerant magnets. *Scientific Reports* **12**, 18987 (2022). URL <https://www.nature.com/articles/s41598-022-20311-7>. Number: 1 Publisher: Nature Publishing Group.
- [12] Zhu, X., Edström, A. & Ederer, C. Magnetic exchange interactions in SrMnO₃. *Physical Review B* **101**, 064401 (2020). URL <https://link.aps.org/doi/10.1103/PhysRevB.101.064401>.
- [13] Solovyev, I. V. & Terakura, K. Effective single-particle potentials for MnO in light of interatomic magnetic interactions: Existing theories and perspectives. *Physical Review B* **58**, 15496–15507 (1998). URL <https://link.aps.org/doi/10.1103/PhysRevB.58.15496>. Publisher: American Physical Society.
- [14] Harashima, Y. et al. Data assimilation method for experimental and first-principles data: Finite-temperature magnetization of (Nd,Pr,La,Ce)₂(Fe,Co,Ni)₁₄B. *Physical Review Materials* **5**, 013806 (2021). URL <https://link.aps.org/doi/10.1103/PhysRevMaterials.5.013806>. Publisher: American Physical Society.
- [15] Antal, A. et al. First-principles calculations of spin interactions and the magnetic ground states of Cr trimers on Au(111). *Physical Review B* **77**, 174429 (2008). URL <https://link.aps.org/doi/10.1103/PhysRevB.77.174429>. Publisher: American Physical Society.
- [16] Togo, A., Shinohara, K. & Tanaka, I. Spglib: a software library for crystal symmetry search (2024). URL <http://arxiv.org/abs/1808.01590>. ArXiv:1808.01590 [cond-mat].
- [17] Heine, M., Hellman, O. & Broido, D. Temperature-dependent renormalization of magnetic interactions by thermal, magnetic, and lattice disorder from first principles. *Physical Review B* **103**, 184409 (2021). URL <https://link.aps.org/doi/10.1103/PhysRevB.103.184409>. Publisher: American Physical Society.
- [18] Sandratskii, L. M. Noncollinear magnetism in itinerant-electron systems: Theory and applications. *Advances in Physics* **47**, 91–160 (1998). URL <https://doi.org/10.1080/000187398243573>. Publisher: Taylor & Francis eprint: <https://doi.org/10.1080/000187398243573>.
- [19] Drautz, R. & Fähnle, M. Spin-cluster expansion: Parametrization of the general adiabatic magnetic energy surface with ab initio accuracy. *Physical Review B* **69**, 104404 (2004). URL <https://link.aps.org/doi/10.1103/PhysRevB.69.104404>. Publisher: American Physical Society.
- [20] Blöchl, P. E. Projector augmented-wave method. *Phys. Rev. B* **50**, 17953–17979 (1994).
- [21] Kresse, G. & Furthmüller, J. Efficient iterative schemes for *ab initio* total-energy calculations using a plane-wave basis set. *Phys. Rev. B* **54**, 11169–11186 (1996).
- [22] Kresse, G. & Joubert, D. From ultrasoft pseudopotentials to the projector augmented-wave method. *Phys. Rev. B* **59**, 1758–1775 (1999).
- [23] Perdew, J. P. et al. Restoring the Density-Gradient Expansion for Exchange in Solids and Surfaces. *Physical Review Letters* **100**, 136406 (2008). URL <https://link.aps.org/doi/10.1103/PhysRevLett.100.136406>. Publisher: American Physical Society.
- [24] Perdew, J. P., Burke, K. & Ernzerhof, M. Generalized Gradient Approximation Made Simple. *Phys. Rev. Lett.* **77**, 3865–3868 (1996).
- [25] Dudarev, S. L., Botton, G. A., Savrasov, S. Y., Humphreys, C. J. & Sutton, A. P. Electron-energy-loss spectra and the structural stability of nickel oxide: An LSDA+U study. *Physical Review B* **57**, 1505–1509 (1998). URL <https://link.aps.org/doi/10.1103/PhysRevB.57.1505>. Publisher: American Physical Society.
- [26] Roux, D. L., Vincent, H., L'Héritier, P. & Fruchart, R. CRYSTALLOGRAPHIC AND MAGNETIC STUDIES OF Nd₂Co₁₄B AND Y₂Co₁₄B. *Journal de Physique Colloques* **46**, C6 (1985). URL <https://hal.science/jpa-00224895>.
- [27] Herbst, J. F., Croat, J. J. & Yelon, W. B. Structural and magnetic properties of Nd₂Fe₁₄B (invited). *Journal of Applied Physics* **57**, 4086–4090 (1985). URL <https://doi.org/10.1063/1.334680>.
- [28] Matsubara, F. & Inawashiro, S. Mixture of Two Anisotropic Antiferromagnets with Different Easy Axes. *Journal of the Physical Society of Japan* **42**, 1529–1537 (1977). URL <https://journals.jps.jp/doi/10.1143/JPSJ.42.1529>. Publisher: The Physical Society of Japan.
- [29] Pizzi, G. et al. Wannier90 as a community code: new features and applications. *Journal of Physics: Condensed Matter* **32**, 165902 (2020). URL <https://dx.doi.org/10.1088/1361-648X/ab51ff>. Publisher: IOP Publishing.
- [30] Akai, H. Fast Korringa-Kohn-Rostoker coherent potential approximation and its application to FCC Ni-Fe systems. *Journal of Physics: Condensed Matter* **1**, 8045 (1989). URL <https://dx.doi.org/10.1088/0953-8984/1/43/006>.
- [31] Rezaei, N., Alaei, M. & Akbarzadeh, H. ESpinS: A program for classical Monte-Carlo simulations of spin systems. *Computational Materials Science* **202**, 110947 (2022). URL <https://www.sciencedirect.com/science/article/pii/S0927025621006431>.
- [32] Edström, A. & Ederer, C. First-principles-based strain and temperature-dependent ferroic phase diagram of SrMnO₃. *Physical Review Materials* **2**, 104409 (2018). URL <https://link.aps.org/doi/10.1103/PhysRevMaterials.2.104409>. Publisher: American Physical Society.
- [33] Maurel, L. et al. Nature of antiferromagnetic order in epitaxially strained multiferroic SrMnO₃ thin films. *Physical Review B* **92**, 024419 (2015). URL <https://link.aps.org/doi/10.1103/PhysRevB.92.024419>. Publisher: American Physical Society.
- [34] Wang, V., Xu, N., Liu, J.-C., Tang, G. & Geng, W.-T. VASPKIT: A user-friendly interface facilitating high-throughput computing and analysis using VASP code. *Computer Physics Communications* **267**, 108033 (2021). URL <https://www.sciencedirect.com/science/>

- article/pii/S0010465521001454.
- [35] Momma, K. & Izumi, F. VESTA 3 for three-dimensional visualization of crystal, volumetric and morphology data. *Journal of Applied Crystallography* **44**, 1272–1276 (2011). URL <https://journals.iucr.org/j/issues/2011/06/00/db5098/>. Publisher: International Union of Crystallography.
- [36] Miyake, T., Harashima, Y., Fukazawa, T. & Akai, H. Understanding and optimization of hard magnetic compounds from first principles. *Science and Technology of Advanced Materials* **22**, 543–556 (2021). URL <https://doi.org/10.1080/14686996.2021.1935314>. Publisher: Taylor & Francis .eprint: <https://doi.org/10.1080/14686996.2021.1935314>.
- [37] Gohda, Y. First-principles determination of intergranular atomic arrangements and magnetic properties in rare-earth permanent magnets. *Science and Technology of Advanced Materials* **22**, 113–123 (2021). URL <https://doi.org/10.1080/14686996.2021.1877092>. Publisher: Taylor & Francis .eprint: <https://doi.org/10.1080/14686996.2021.1877092>.
- [38] Seo, I., Tanaka, S., Endo, M. & Gohda, Y. Prediction of NdFe₁₆-based permanent-magnet compounds with high magnetization. *Applied Physics Express* **17**, 075502 (2024). URL <https://dx.doi.org/10.35848/1882-0786/ad5fd9>. Publisher: IOP Publishing.
- [39] Sagawa, M., Fujimura, S., Togawa, N., Yamamoto, H. & Matsuura, Y. New material for permanent magnets on a base of Nd and Fe (invited). *Journal of Applied Physics* **55**, 2083–2087 (1984). URL <https://doi.org/10.1063/1.333572>.
- [40] Fuerst, C. D. & Herbst, J. F. Hard magnetic properties of Nd-Co-B materials. *Journal of Applied Physics* **64**, 1332–1337 (1988). URL <https://doi.org/10.1063/1.341855>.
- [41] Tsuna, S. & Gohda, Y. First-principles phonon calculations of neodymium-magnet compounds. *Journal of Applied Physics* **133**, 115103 (2023). URL <https://doi.org/10.1063/5.0142945>.
- [42] Tanaka, T. & Gohda, Y. Prediction of the Curie temperature considering the dependence of the phonon free energy on magnetic states. *npj Computational Materials* **6**, 1–7 (2020). URL <https://www.nature.com/articles/s41524-020-00458-5>. Publisher: Nature Publishing Group.
- [43] Mankovsky, S., Polesya, S. & Ebert, H. Extension of the standard Heisenberg Hamiltonian to multi-spin exchange interactions. *Physical Review B* **101**, 174401 (2020). URL <https://link.aps.org/doi/10.1103/PhysRevB.101.174401>. Publisher: American Physical Society.
- [44] Antropov, V. P. The exchange coupling and spin waves in metallic magnets: removal of the long-wave approximation. *Journal of Magnetism and Magnetic Materials* **262**, L192–L197 (2003). URL <https://www.sciencedirect.com/science/article/pii/S0304885303002063>.
- [45] Haynes, W. (ed.) *CRC Handbook of Chemistry and Physics* (CRC Press, 2014), 95th edn.
- [46] Fawcett, E. Spin-density-wave antiferromagnetism in chromium. *Reviews of Modern Physics* **60**, 209–283 (1988). URL <https://link.aps.org/doi/10.1103/RevModPhys.60.209>. Publisher: American Physical Society.
- [47] Tanaka, T. & Gohda, Y. First-Principles Study of Magnetism-Dependent Phonons Governed by Exchange Ligand Field. *Journal of the Physical Society of Japan* **89**, 093705 (2020). URL <https://journals.jps.jp/doi/10.7566/JPSJ.89.093705>. Publisher: The Physical Society of Japan.